Quantifying the impact of mitral valve anatomy on clinical markers using surrogate models and sensitivity analysis

Jan-Niklas Thiel[1] Joel Gestrich[1] Ulrich Steinseifer[1] Ingeborg Friehs[2]
Daniel Diaz-Gil[2] Michael Neidlin[1]

[1]Department of Cardiovascular Engineering, Institute of Applied Medical Engineering
Medical Faculty, RWTH Aachen University, Aachen, Germany

[2]Department of Cardiac Surgery, Boston Children's Hospital, Boston, USA

neidlin@ame.rwth-aachen.de

June 25, 2024

Abstract

Blood flow studies within the left ventricle have proven to be promising for future clinical decision-making. However, accurate segmentation of heart valves, particularly the mitral valve, is still challenging. The MV has a significant impact on local flow phenomena within the ventricle and assumptions on its anatomy and location introduce uncertainties that are not yet fully understood. The overall aim of this study is to quantify the impact of uncertainty in defining MV anatomy and location on local and global clinical outcomes, such as kinetic energy, energy loss, transventricular pressure gradient and locally resolved wall shear stresses. We use a combination of computational fluid dynamics moving mesh simulations of cardiac blood flow, reduced order modeling (ROM) and variance-based global sensitivity analysis (GSA). We uncover a non-linear relationship between geometrical uncertainties and flow biomarkers with mitral valve size and angle as the most important parameters. Uncertainty quantification of echocardiography measurements reveals a standard deviation between 5-30% for the different output markers. We further outline the importance of robust ROM and GSA as model choice can drastically influence the results. Our entire pipeline is summarized in the open source tool **SASQUATCH** - a framework for sensitivity analysis and uncertainty quantification in cardiac hemodynamics.

Keywords: Cardiac blood flow; Computational fluid dynamics; Reduced order modeling; Global sensitivity analysis; Uncertainty quantification

1 Introduction

The blood flow within the ventricle is tightly related to cardiac function and knowledge about the hemodynamics can be used as a marker of ventricular health [20]. More specifically, markers derived from the blood flow structures such as vortex dynamics, energy dissipation and pressure gradients have the potential to serve as parameters to support clinical decision making [5, 15]. Computational cardiac models created from non-invasive imaging data can provide this information on a patient-specific basis. Recent advances in cardiovascular imaging, such as time-resolved magnetic resonance imaging (4D MRI) and real-time three-dimensional echocardiography (RT3DE), gave rise to a large

amount of Computational Fluid Dynamics (CFD) models of ventricular hemodynamics [25, 6, 18, 14, 4, 2] focusing on the intriguing role of the intraventricular flow features and their relation to the cardiac physiology. An important aspect of all computational models is the uncertainty of the model predictions and uncertainty quantification (UQ) is a key aspect to ensure model credibility [24]. There are various sources of uncertainties which can be for instance stem from variation in the experimental data, errors in the modeling processes or uncertainties introduced by the computational algorithms. An extensive overview of UQ with important terminology is presented by Roy and Oberkampf [22].

In many models, the movement of the ventricular walls and the geometry of the valves is extracted from the imaging data and simulation models are performed using these inputs. In particular, the atrioventricular valves, in the case of left ventricular blood flow, the mitral valve (MV), are extremely difficult to model due to the complexity of their anatomy and movement. The location of the mitral annulus, the size of the MV and its angularity are all known to influence cardiac hemodynamics [26] and its geometry has thus a critical importance in all cardiac hemodynamics models. Particularly during pediatric and neonatal applications, such as blood flow simulations in congenital heart diseases (CHDs) [17], the influence of the imaging modality on the model output can be critical due to the small geometries at hand. Furthermore, in the neonatal and pediatric context, echocardiography, more specifically real-time three-dimensional echocardiography (RT3DE), is often used. RT3DE is fast, reproducible and non-invasive, however it can reach its limits during analysis of small anatomical structures. Computational models using RT3DE exist in the pediatric, neonatal and fetal context [17, 29]. Thus, quantifying the influence of geometrical uncertainties on fluid dynamics markers is important to further improve the modeling and patient-specific planning in fetal, neonatal and pediatric cardiology.

The general approach of UQ consists of Monte Carlo simulations of variations of the input parameters, within specified limits, and the statistical analysis of the resulting output variations. Further on, global sensitivity analysis (GSA) is performed to obtain an overarching view on model behavior [27]. This requires many model evaluations, which poses an unfeasible computational burden in the context of CFD simulations. For this reason, surrogate models are employed here for approximation. Until now, the relationship between the geometrical assessment of the MV dimensions and the occurring ventricular hemodynamics has not been analyzed in a systematic way. In our work, we investigate the influence of the MV geometry on cardiac hemodynamics and quantify the uncertainty of widely used flow-based markers of cardiac function. We do so through a combination of RT3DE-based CFD simulations of cardiac blood flow, surrogate modeling, and global sensitivity analysis.

2 Methods

An overview of the approach is shown in Figure 1. At first, CFD simulations of an already established ventricular hemodynamics model using the moving methodology are performed. The four geometrical mitral valve parameters y_d, z_d, α, and R_L are varied to create n=80 CFD results for the studied parameter range. In the second step, markers from the flow data are extracted. These include spatially and temporally averaged markers E_{loss}, E_{kin}, and $TVPG$ as well as the spatially resolved WSS. This step also includes analysis of the calculated data to check for outliers and errors in the dataset. In the third step, different reduced order models (ROMs) that create the relationship between the geometrical input parameters and the flow derived outputs are evaluated and the best performing ROM is chosen. This ROM is then selected to perform a global sensitivity

analysis (GSA) together with uncertainity quantification (UQ) on the influence of the mitral valve geometrical parameters on ventricular hemodynamics.

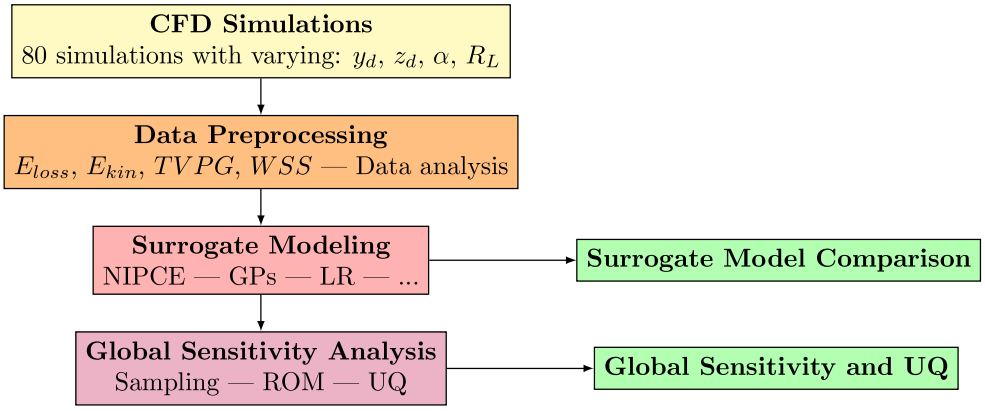

Figure 1: Flowchart of approach.

2.1 Data generation

Intraventricular blood flow was determined from moving mesh simulations based on three-dimensional real-time echocardiography recordings. A neonatal subject with an ESV of 7.2 ml, an EDV of 17.1 ml, and a heart rate of 116 bpm was selected. In brief, segmented ventricular deformations were extracted from the clinical data and movement of the computational mesh was imposed according to these deformation. For more details on the algorithms, please see our previous work in [10]. In addition to the study cited above, a left atrium and a aortic root were scaled to the aortic and mitral valve (MV) respectively and added to the ventricle. At last, the mitral and aortic valves were modeled as porous media as explained in [28]. An unstructured mesh with approx. 2 mio elements was chosen and laminar simulations with a Newtonian blood model $\rho = 1056.4[kg/m^3]$ and $\eta = 3.6mPas$ was set. A pressure-based solver and 5 cardiac cycles with 240 time steps per cycle were chosen. Both inlet and outlet have constant pressure profiles. All simulations were performed with ANSYS Fluent 2021R2 (Ansys Inc. Gettysburg, USA). The creation of simulation setups has been automated to minimise user input and drastically reduce preparation time. A reference setup with all scripts for automation can be found at `https://doi.org/10.5281/zenodo.12519189`.

An in-house automated pipeline was used to extract the patient-specific ventricular geometry and perturb them along Table 1. It streamlines and enhances the quality of the pre-processing, which includes attaching anatomical parts such as the aorta, atrium, valves to the patient specific ventricle. The reconstruction pipeline can be found on Github at `https://github.com/DanielVerhuls/Ventricle-reconstruction-pipeline`.

Left side of Figure 2 shows the cross-section of the ventricle with four geometrical parameters y_d, z_d, α, R_L, which describe the size and location of the MV. y_d and z_d describe the displacement of the MV with respect to the ventricular apex. α is the angle of the MV in the anterio-posterior plane and influences the propagation of the mitral jet. At last, R_L is half the MV "long axis", which can be seen on the right of Figure 2. The short axis of MV is scaled accordingly so that the initial ratio to R_L remains unchanged. A geometrical uncertainty of $\pm 2mm$ was assumed according to [30]. This resulted in the variations as outlined in Table 1. Hypercube sampling was used to create n=80 training simulations that covered the parameter space from Table 1.

Parameter	Minimum	Maximum	Variation absolute
y_d	-7mm	-3mm	133.33%
z_d	49mm	53mm	8.16%
α	-10°	+10°	-
R_L	2.6mm	4.6mm	76.92%

Table 1: Input perturbation bounds derived from the geometric uncertainty.

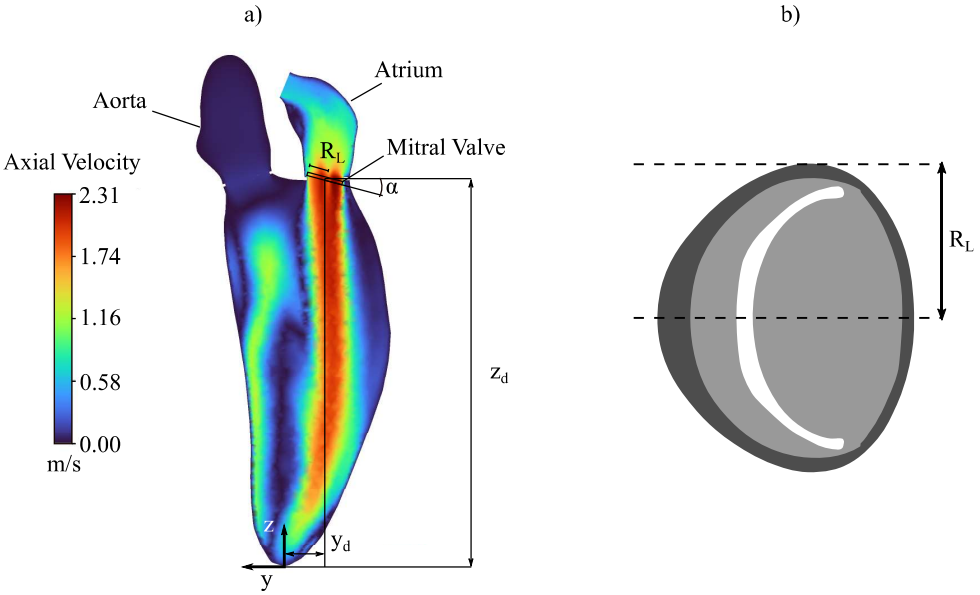

Figure 2: Velocity field of left ventricle with annotations geometrical parameters used as inputs for the surrogate models in a). Top view showing the shape of the MV with the MV long axis in b).

2.2 Data preprocessing

Based on the last cycle of the CFD data, the following four markers were determined - Energy loss (E_{loss}), kinetic energy (E_{kin}), transventricular pressure gradient ($TVPG$) and wall shear stress (WSS).

Energy loss and kinetic energy describe the pumping efficiency of the heart. In the physiological state, a stable vortex is formed during diastolic filling that is then ejected during systole [20]. Cardiac pathologies can lead to abnormal vortex shapes connected to high energy losses and low kinetic energies as has been shown for adult and pediatric subjects in vivo [8, 17, 23]. Both are defined as

$$E_{loss} = \mu \int_{\Omega} \Phi dV \tag{1}$$

$$E_{kin} = \frac{1}{2} \int_{\Omega} \rho v^2 dV \tag{2}$$

where μ defines the dynamic viscosity, Φ the energy dissipation, ρ the fluid density and Ω the fluid space.

The transventricular (or intraventricular) pressure gradient TVPG is another important parameter to assess the functional capacity of the heart and has been applied in the detection of ventricular impairment [19, 7]:

$$TVPG = P_{apex} - P_{basal} \tag{3}$$

where P_{basal} is the pressure near the inflow (87.5% of ventricular height) and P_{apex} the pressure at the apex (15% of ventricle height).

At last, the time-averaged wall shear stress (WSS) was determined at the ventricular wall. The WSS describes the interaction between the blood and the endothelial cells and has been identified as a driving marker in many processes of vascular pathophysiology such as tissue remodeling or atherosclerosis [9]. To consider the various zones of the ventricular wall and their different WSS measurements, the left ventricle was divided into 17 segments as suggested by the American Heart Association [16] and projected onto a 2D plane as shown in Figure 3.

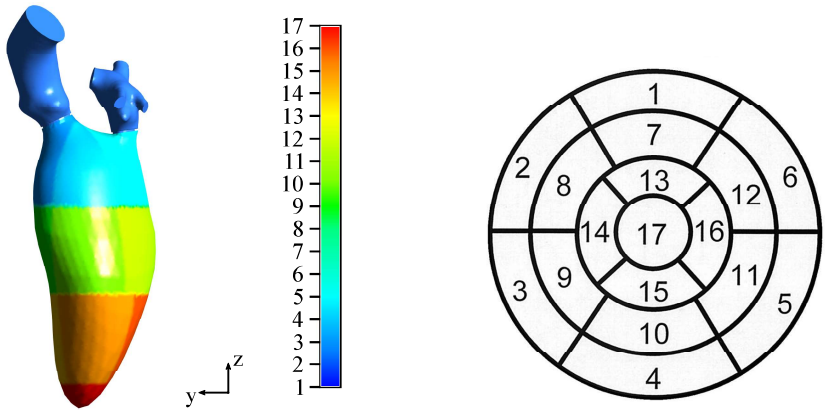

Figure 3: 17 segments representation of the left ventricle in 3D and 2D adapted from [16].

Before surrogate modeling was performed, pairwise correlation and histograms were used to assess the quality of the data and scan for outliers and errors.

2.3 Surrogate modeling

In this work, five different ROMs were tested regarding their prediction quality and efficiency. In general, the relationship

$$y = g(\beta, x) \tag{4}$$

with $\beta_i \in \mathbb{R}$ being function specific parameters of g, input parameter $x = (x_1, x_2, ..., x_n)$ and output parameter $y = (y_1, y_2, ..., y_m)$ was used to find the best performing model. In our case $x = (y_d, z_d, \alpha, R_L)$ and $y = (WSS, E_{loss}, E_{kin}, TVPG, wss_1, ..., wss_{17})$, which gives $n = 4$ and $m = 21$. WSS_i is the local wall shear stress for each segment, while WSS is the average of all segments.

Linear Regression Model A generalized linear model (LR) was trained according the following equation and the β_i were identified:

$$g(x) = \beta_0 + \sum_{i=1}^{n} \beta_i x_i \tag{5}$$

Gaussian Process A Gaussian process (GP) was used to describe the relationship between input and output:

$$g(x) = p^T(x)\beta + Z(x) \tag{6}$$

The polynomial basis function is given by $p(x) = (p_1(x), ..., p_M(x))$. Again β_i are the model parameters, and $Z(x)$ is a Gaussian process, also known as kernel function.

Matérn kernels, that are a generalization of radial basis functions, have been used according to the equation below:

$$k(x_i, x_j) = \frac{1}{\Gamma(\nu)2^{\nu-1}}(\frac{\sqrt{2\nu}}{l}r)^\nu K_\nu(\frac{\sqrt{2\nu}}{l}r) \tag{7}$$

with a modified Bessel function $K_\nu(\cdot)$ [1] and the gamma function $\Gamma(\cdot)$. The parameter ν controls the smoothness of the learned function and was set as $\nu = 0.5$ [13]. The length scale of the kernel was set according to the parameter bounds.

Non Intrusive Polynomial Chaos Expansion The general idea of Non Intrusive Polynomial Chaos Expansion (NIPCE) is to represent the output as a polynomial expansion orthogonal to a probability distribution. For multivariate expansions, the tensor product of univariate expansions is usually used. The formula for NIPCE is given by:

$$g(x) = \sum_{0 \leq |\alpha| \leq p} \omega_\alpha \Psi_\alpha(x), |\alpha| = \sum_{i=1}^{n} \alpha_i \tag{8}$$

where $\alpha = \{\alpha_1, ...\alpha_n\} | \alpha_i \geq 0$ is the multidimensional index notation vector. ω_α is the coefficient vector weighting the respective basis function Ψ_α which is itself a multivariate polynomial vector. The parameter p represents the maximum polynomial degree of the expansion. It is chosen depending on the complexity of the function, the data set, and its size. Hosder et al. suggests using

$$p = 2\frac{(n_{pol} + n_{dim})!}{n_{pol}! n_{dim}!} \tag{9}$$

with an oversampling parameter ≥ 2 where n_{pol} is the number of polynomials in the chaos expansion and n_{dim} is the order of input dimensions [12].

With a number of simulations of $n_{sim} = 80$ and a number of input parameters of $n_{dim} = 4$, a reasonable choice according to equation 9, is an order of 2 or 3 [3]. Both orders have been tested. For the generation of its expansion, a uniform distribution with all input parameter bounds was chosen.

k-Nearest Neighbors and Random Forest At last, two other surrogate models, that are not typically used in the context of sensitivity analysis and UQ were used as a benchmark. k-Nearest Neighbors (KN) predicts the output by aggregating the k nearest neighbors of already learned input-output pairs. Random Forests (RF) fits decision tree regressors to random subsets of the data, which together form a random forest.

2.4 Training, Testing and Evaluation of ROMs

Training and testing were performed using k-fold cross validation with $k = 10$ random, equally sized splits. R^2 and $MAPE$ were used to evaluate the accuracy of the models according to the equations

$$MSE = \frac{1}{n}\sum_{i=1}^{n}(y_{i,actual} - y_{i,predicted})^2, \tag{10}$$

$$R^2 = 1 - \frac{MSE}{\sigma^2}, \tag{11}$$

$$MAPE = \frac{1}{n}\sum_{i=1}^{n}\frac{|y_{i,actual} - y_{i,predicted}|}{max(\epsilon, y_{i,actual})} \tag{12}$$

with n being the number of samples and y the output values and $\epsilon > 0$ is arbitrarily small to avoid undefined results for $max(y_{i,predicted}) = 0$, σ is the standard deviation.

2.5 Global sensitivity analysis

Variance-based global sensitivity analysis (GSA) through the computation of Sobol indices was performed. The first order indices are given by

$$S_i^1 = \frac{V_i}{V(y)} = \frac{V_{x_i}[E_{x_{\neg i}}(y|x_i)]}{V(y)} \tag{13}$$

They are restricted to the contribution of a single input parameter, second order to the combination of two, and so on. It holds:

$$\sum_{i=1}^{d} S_i^1 + \sum_{i<j}^{d} S_{ij}^2 + ...S_{12...d}^d = 1 \tag{14}$$

Total order indices include the full contribution of each input variable and combine direct and indirect interaction effects [21] and are calculated with the formula given by Homma and Saltelli [11]:

$$ST_i = \frac{V_{x_{\neg i}}(E_{x_{\neg i}}(Y|x_{\neg i}))}{V(y)} \tag{15}$$

The larger S, the greater the influence of each input on the output. The best performing ROM was used to generate $2^9 \times (2n_{dim} + 2) = 5120$ samples as input data for the GSA, which yields converged Total order indices S_T.

2.6 Implementation of SASQUATCH

The methods presented above were implemented in Python and are made freely available through https://github.com/nikithiel/SASQUATCH. The package *SASQUATCH*, which stands for **S**ensitivity **A**nalysis and Uncertainty **QUA**n**T**ification in **C**ardiac **H**emodynamics provides a variety of tools to perform global sensitivity analysis and uncertainty quantification using existing simulation data. It consists of three parts. The data analysis part checks for outliers and errors in the simulation data and helps to understand the relationships between the input-output pairs using histograms and correlation plots. The surrogate modeling part allows to implement and benchmark reduced order models such as the ones presented in the manuscript. Other ROMs can be easily added. At last, global sensitivity analysis through Sobol indices can be executed, the results visualized and the input uncertainties can be propagated through the models. **SASQUATCH** uses *Sklearn*, *Chaospy*, *Pandas*, and *SALib*. Supported input file formats are the *Ansys Fluent* output *.out*, *.xlsx*, or *.csv*.

3 Results

3.1 Analysis of CFD data

The Spearman pairwise correlation for the input and output data is shown in Figure 4. No outliers can be observed and the data points are spread over the sampling space as defined in Table 1. A high influence of R_L on all output markers can be observed. Relationships between other input and output parameters are not observable. Histograms of the individual outputs are presented in Supplementary Figure S1 for all 21 output values.

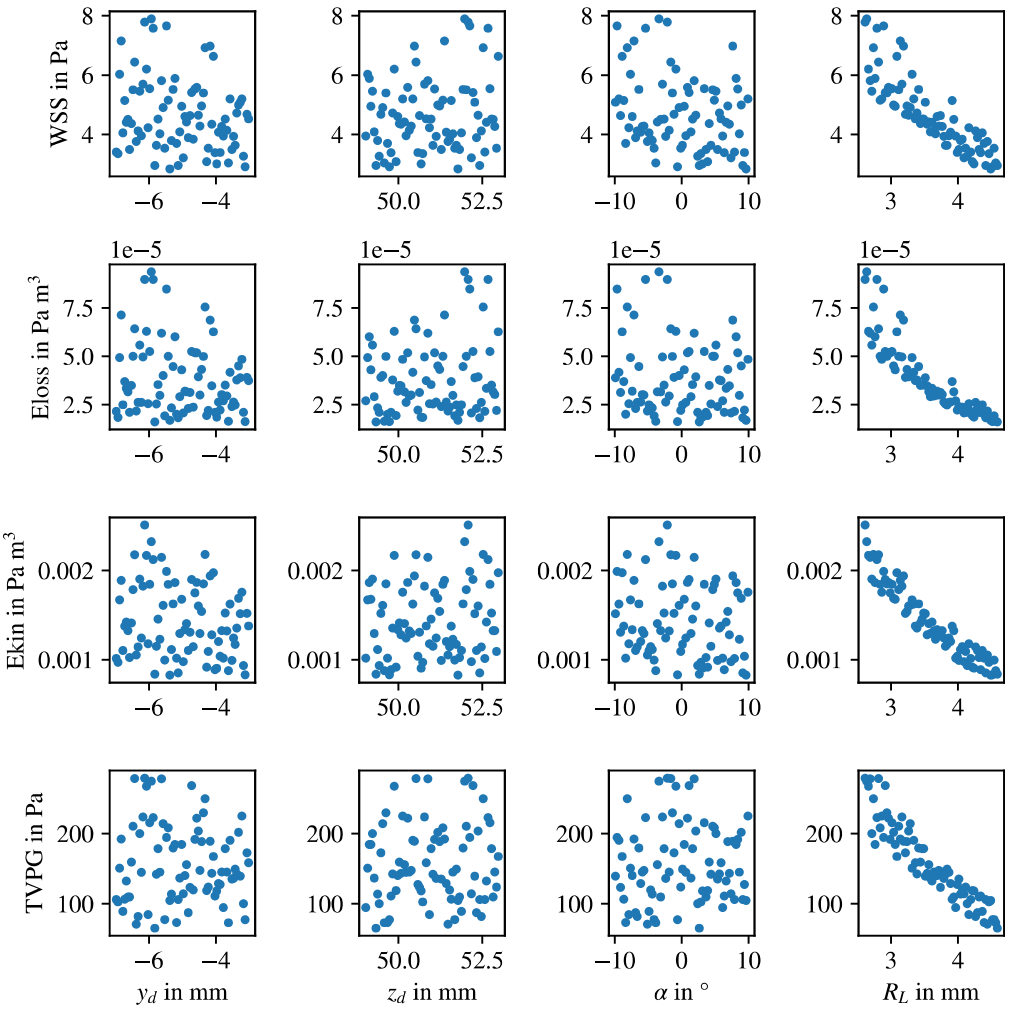

Figure 4: Scatterplot of input and output parameters.

More details about the maximum and minimum values, as well as the percentage variation, is shown in Table 2. The values indicate a large variation for the output, ranging from 177.75% for WSS to 486.63% for E_{loss} and a non-linear relationship between input and output variations.

	$WSS\ [Pa]$	$E_{loss}\ [J]$	$E_{kin}\ [J]$	$TVPG\ [Pa]$
Minimum	2.84	$1.6e^{-5}$	$8.27e^{-4}$	65.25
Maximum	7.9	$8.49e^{-5}$	$2.51e^{-3}$	279.07
Variation	177.75%	431.26%	203.63%	327.69%

Table 2: Minimum, maximum, and variation in output distribution.

3.2 Performance evaluation of surrogate models

Figure 5 shows the R^2 score and MAPE for all ROM using k-fold cross validation. The black bars indicate the standard deviation over all folds and output parameters. The best R^2 score has *NIPCE* and *GP* with almost 0.7, then *LR* and *RF* with about 0.6 and lastly *kNN* with 0.2. Model evaluation using MAPE shows similar results.

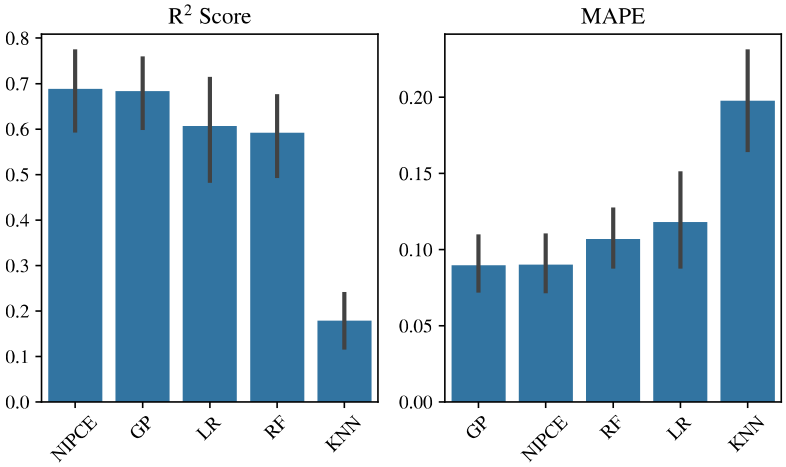

Figure 5: Mean of R^2 Scores and MAPE over all folds and output parameters.

The influence of ROM hyperparameters on the prediction quality has been evaluated as well. More specifically, the R^2 scores of the *NIPCE* for different polynomial orders yield the order 2 as the best performing one, as can be seen on the left side of Supplementary Figure S2). Different smoothing parameters ν of the kernel function in equation 7 have been evaluated in Supplementary Figure S2 right side. The value of $\nu = 0.5$ was chosen because it performs well and is much cheaper from a computational point of view, with $10x$ faster run times compared to the best performing smoothing factor $\nu = 0.3$.

A detailed insight on the ROM performance is shown with probability density functions (PDF) for each output marker and three surrogate models *NIPCE*, *GP*, and *LR* in Figure 6. Skewed distributions are seen in all training data. This leads to poor performance of *LR* at the outer bounds, for instance for $TVPG$ or WSS_{16}. Other values, such as WSS_1 or WSS_2 can be predicted quite well, even by *LR*. The *GP* model sometimes "overshoots" the density plots at the maxima, for instance for WSS_{16} and WSS_{11}. *NIPCE* seems to match the PDFs quite well, however deviations for PDFs can also be observed. *NIPCE* is selected as the ROM for GSA and UQ, however *GP* could also be used as there is no definite outperformance of one surrogate model against the other.

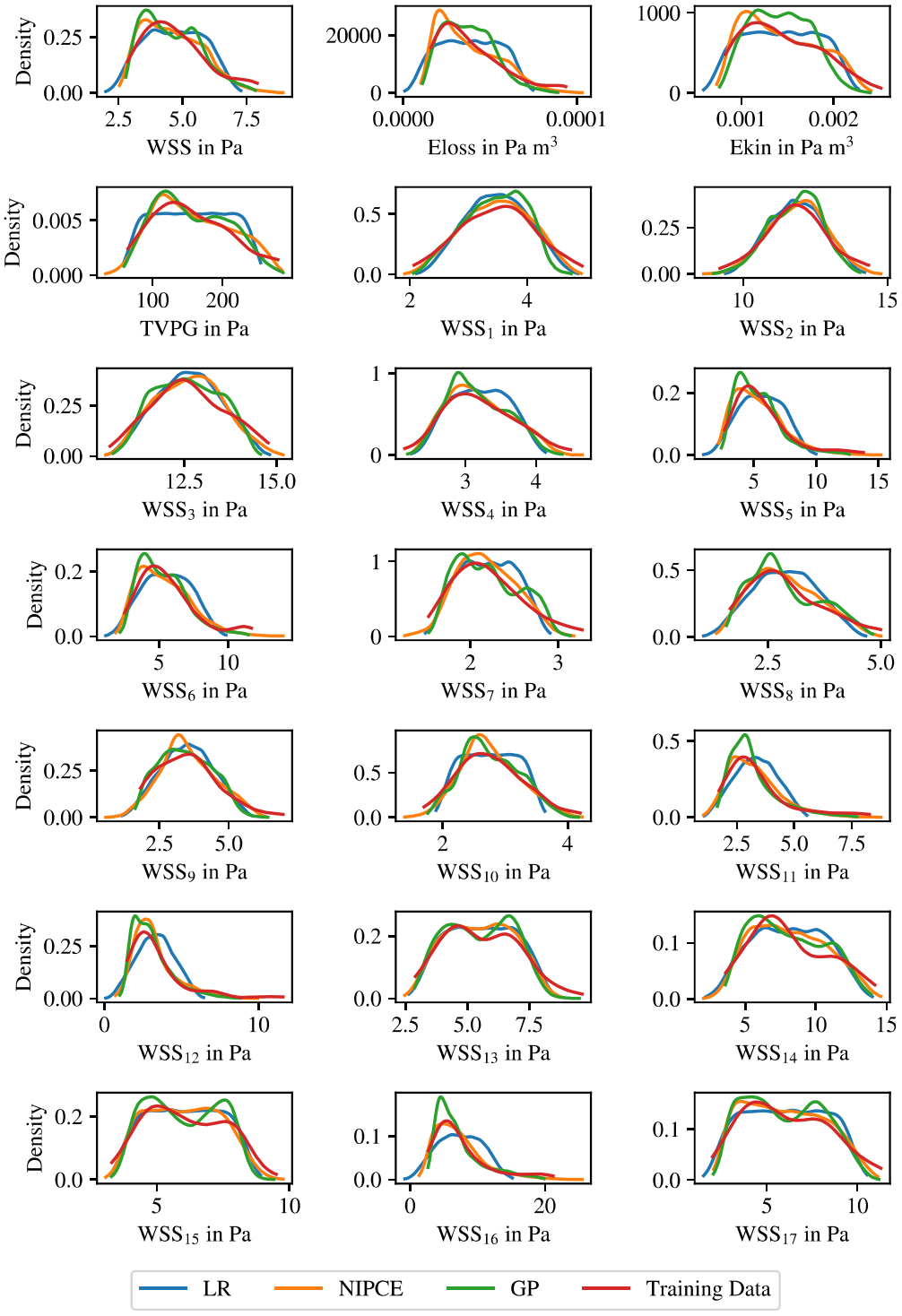

Figure 6: Density plot of *LR*, *NIPCE*, *GP*, and training data.

3.3 Global sensitivity analysis and uncertainty quantification

GSA

The results of the GSA are presented in Figure **??**. The left side shows total order sensitivity indices for all output values in a heatmap. The right side shows the total order sensitivity indices for WSS using the 17-segment visualization of the ventricle. The entire input parameter range, as shown in Table 1 has been used to produce these results

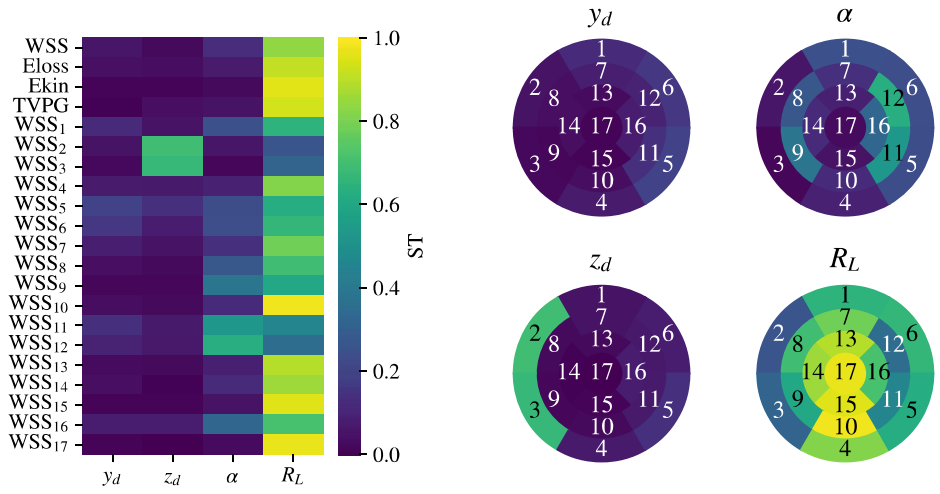

Figure 7: Total order sensitivities S_T heatmap for all cardiac output metrics on the left and locally resolved WSS using 17-segment visualization on the right. Results obtained using *NIPCE*.

The largest influence on all output metrics has the parameter R_L, the radius of the mitral valve "long axis". The MV angle α has little influence on the spatially averaged metrics and large influence on the WSS with large variations between the individual segments. For instance, WSS_{11} and WSS_{12}, which are the inferolateral and anterolateral segments in the middle region of the ventricle have $S_T > 0.5$ while the basal inferoseptal and anteroseptal regions (WSS_2 and WSS_3) are not sensitive to the angle. Interestingly, the y orientation of the MV annular plane y_d does not have a strong influence on any results and only WSS_2 and WSS_3 are influenced by z_d. Similar behaviour has been observed with the GP and LR models (results not shown).

In the next step, we wanted to investigate the influence of input parameter variation range on the total order sensitivity indices. Thus, the GSA was performed with an increasing level of variations between $0mm$ and $1.26mm$. The variation of the angle α was determined from trigonometry as $u_\alpha = arcsin(\frac{u_m}{\sqrt{(R_L^2+u_m^2)}})$ with u_α being the uncertainty of the angle and u_m the uncertainty of the measurement. The upper range of $1.26mm$ was computed from the maximum angle variation of 10 deg. The results are presented in Figure 8.

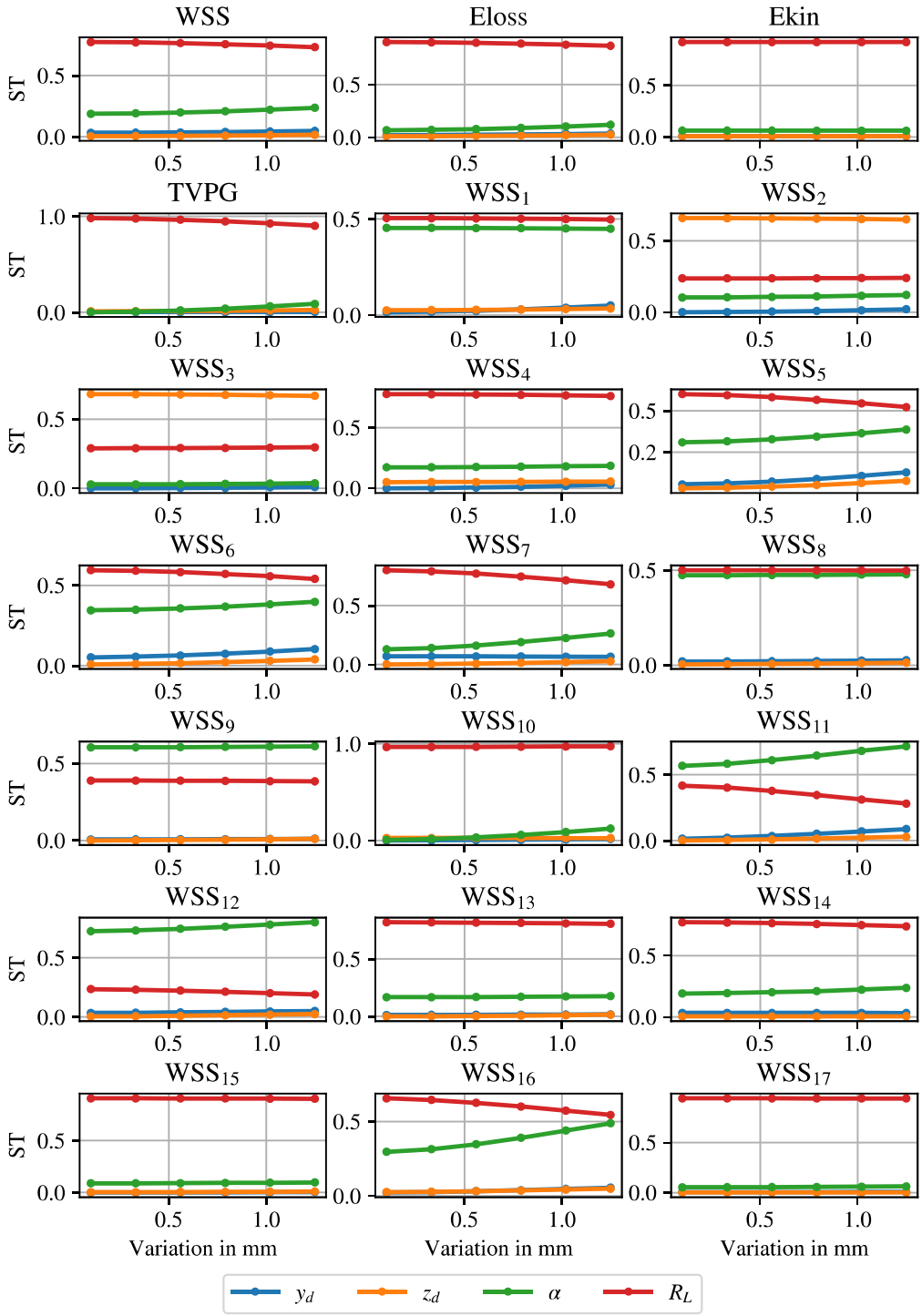

Figure 8: Total order sensitivity values for all output parameters with varying input uncertainty in mm on the x-axes using *NIPCE*.

The figure shows that for most of the output values and most of the variations, the order of the total sensitivity indices stays the same with R_L being the most influential parameter, followed by the angle α. However, in some cases trends and changes in the sensitivities can be observed. For instance, WSS_{16} sensitivity to R_L decreases with increasing variation while the sensitivity towards α is increasing. For most of the investigated output parameters, the sensitivities are independent of the input variation range. It has to be emphasized, that the results in Figure 8 have been created using the *NIPCE* model. A similar investigation with *GP* shows a more complex picture, see Supplementary Figure S3. For several output parameters, spatially resolved as well as spatially averaged ones, the sensitivity indices depend on the input variation range and a change in the order (most sensitive to least sensitive input parameter) might even change.

UQ

In the last step, we wanted to quantify the influence of combined input parameter uncertainties on the output markers. The entire input parameter range from Table 1 has been used. The results in Table 3 are presented for WSS, E_{loss}, E_{kin}, and $TVPG$.

	WSS $[Pa]$	E_{loss} $[J]$	E_{kin} $[J]$	$TVPG$ $[Pa]$
Variation	201.2%	782.5%	195.4%	655%

Table 3: Variation in output parameters based on all possible input parameter uncertainties.

The results exhibit a huge variation with E_{loss} going up close to 800%, $TVPG$ up to around 700%, E_{kin} and WSS up to 200%. It has to be noted, that this analysis presents the "worst case scenario" that is probably not very common in reality as maximal errors in the individual parameter measurements have to be made in such a way that they reinforce their effect on the output markers.
For a more realistic quantification of uncertainty, we thus suggest to focus on the mean and the standard deviation (SD) of the outputs considering input parameter variations. The results are presented in Figure 9 and show the mean and SD with a solid line and bands, respectively. On the x-axes, the input parameter variation is plotted to quantify the influence of lower input parameter variation (0.5 instead of 1 mm) on the output uncertainties.

The plot reads as follows: For a geometrical input uncertainty of 1.26 mm, the $TVPG$ has a standard deviation of 22% and an absolute range of 35 Pa. Reducing the input uncertainty to 0.5 mm leads to a standard deviation of 9% and an absolute uncertainty band of 15 Pa. Overall, different output parameters have different sensitivities to the input variation with SD between 5-30% and we see a non-linear relationship between input uncertainty and output uncertainty. For further evaluation of the individual values, the data is presented in the Supplementary Tables S1 and S2.

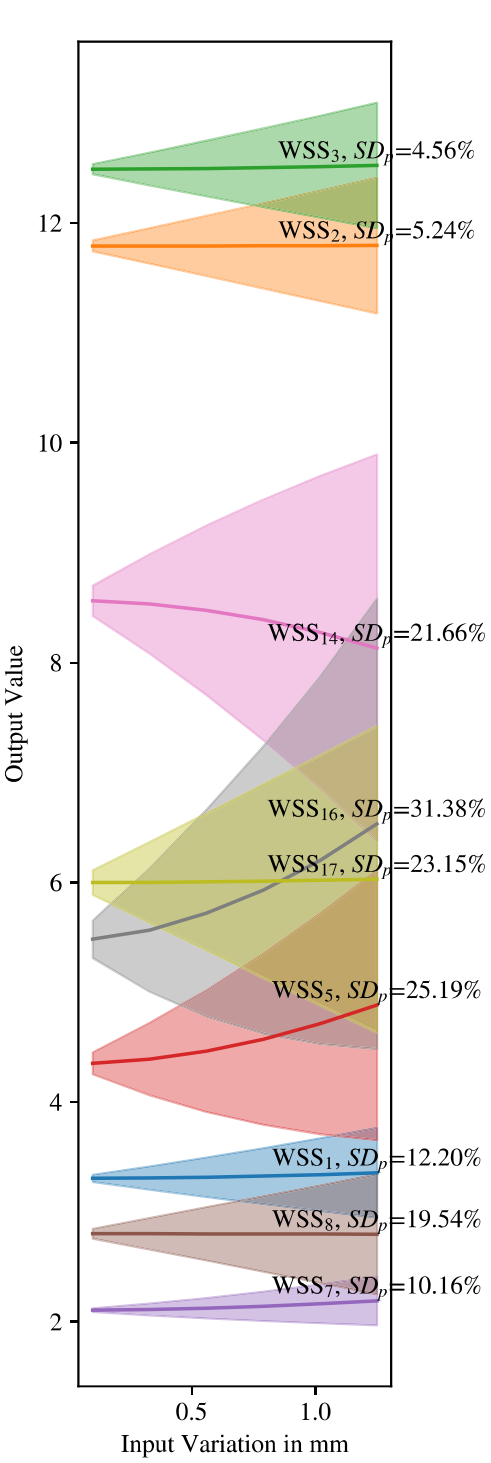

(a) WSS_i in Pa

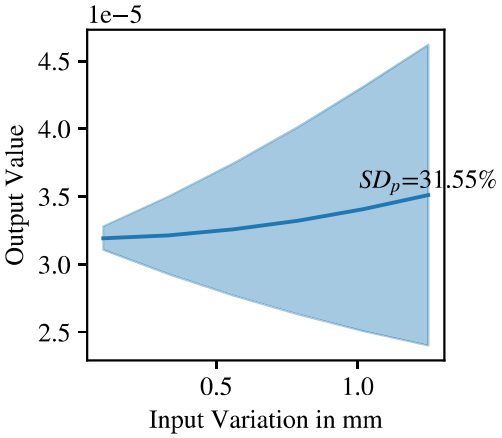

(b) E_{loss} in J

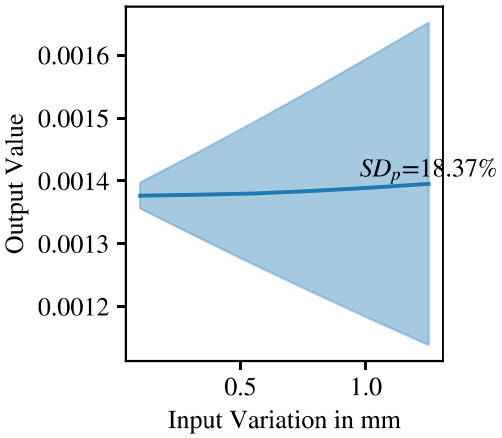

(c) E_{kin} in J

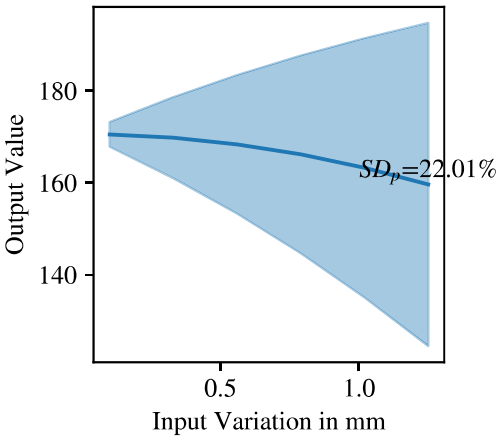

(d) $TVPG$ in Pa

Figure 9: Standard deviation of outputs over different input ranges in mm.

4 Discussion

Sensitivity analysis and uncertainty quantification are two important aspects to increase the credibility of computational models. Within this work, we have used a combination of patient-specific cardiac blood flow simulations, surrogate modeling and variance-based sensitivity analysis to quantify the impact of mitral valve anatomy on clinical markers derived from blood flow fields. We have varied 4 geometrical parameters y_d, z_d, α and R_L and extracted 21 markers (E_{kin}, E_{loss}, $TVPG$ and both averaged and locally resolved WSS at ventricular regions) from 80 CFD simulations. Then, different ROM were trained and assessed in order to perform GSA and UQ using this data.

The training simulations delivered a wide range of output parameters with skewed distributions and variations between 200-400%. Capturing these distributions is possible through surrogate models and NIPCE and GP, two widely used approaches, are able to create the input-output relationship in a reliable manner with R^2 of around 0.7. Investigations of the individual output parameter distributions uncovered differences between ROM and CFD ground truth data with increasing deviations at local maxima of the data. Increasing the polynomial order of NIPCE might be able to better describe the training data, however an increased polynomial order also requires a larger amount of simulations. With the existing 80 simulations, the polynomial order of 2 outperformed other NIPCE approaches. Other surrogate models such as artificial neural networks or support vector machines might also be possible candidates for ROMs in this context. GSA using Sobol indices has emphasized the importance of mitral valve radius R_L and the angle α on the model outputs. With the radius being the most important parameter. Moreover, looking at individual segments of the WSS in the well-known 17-segment model has shown that the sensitivities are regionally dependent. This is not surprising, as WSS is caused by the interaction between the ventricular wall and the mitral jet and its orientation depends on the location and size of the MV. Interestingly, the position of the MV annulus (y_d and z_d) did not have strong influences on the results with some exceptions of the regional WSS. This means, that exact measurement of the MV angularity and size is more important than the annulus position. This in turn means that including the annular movement in ventricular hemodynamics studies might not be that important, particularly when the focus of the study is on the energy loss (E_{loss}) or kinetic energy (E_{kin}). Similar total order sensitivities have been obtained with the GP and LR models. This is a good finding, as it makes the results more independent from the choice of the surrogate model.

The next important observation was the influence of the input parameter variation on the total sensitivity indices. While NIPCE had mostly constant sensitivities throughout the parameter variation range, the sensitivities derived from the GP changed with increasing parameter variation (see Supplementary Figure S3). Moreover, the ranking of most sensitive to least sensitive input parameters changed with different variation ranges. As such, at least for our application presented herein, we see the NIPCE as a more robust surrogate model than GP and want to further stress the importance to perform GSA not only for one input parameter variation but for a range of variations.

At last, the geometrical uncertainties were propagated through the surrogate model. Once again, an increasing range of input parameter variation was selected to quantify the effect of more exact measurements on the output data. Taken together, standard deviations between 5-30% have been observed for the largest variation of 1.26 mm and ± 10 deg. These variations can be reduced with an increased precision in a non-linear manner. On this front, it is interesting to mention that the mean value of some parameters (e.g. E_{kin}) does not change over an increased input parameter variation (however the SD of the mean values increases).

Within this study we have focused on ventricular blood flow in one neonatal subject with an end-diastolic volume of 17ml. Any geometrical variation in such as small anatomy will have drastic effect on the outputs as is also evident from our results. An investigation of adult ventricular blood flow would be of interest to see whether our findings are translatable to other geometries. Although we would expect smaller absolute variations, there is no reason to believe that the relations between the input parameters and the general observations would change.

The ground truth CFD model itself has some limitations. At first, the mitral valve was modeled as a porous medium which is an abstract representation of the real valve. However, including an FSI for 80 simulations is computationally infeasible, particularly considering instabilities of such simulations and difficulties in automated simulations. In addition, the atrium and aortic root were not patient specific but taken from existing data and scaled to our case. On this front, more realistic geometries could increase the patient-specificity of the model.

To perform the calculations, we have used our recently developed interactive pipeline developed using *Python*, which can be found on `https://github.com/DanielVerhuls/Ventricle-reconstruction-pipeline`. It allowed us to automate all steps from geometry pre-processing, setup creation, meshing and simulation and is a first proof of the robustness of the abovementioned pipeline.

5 Conclusion

Taken together, within this study, we have performed a comprehensive sensitivity analysis and quantification of geometrical uncertainties on ventricular hemodynamics in a patient-specific model. The main findings are:

- Non-linear influence of geometrical parameters on common output metrics.
- Different surrogate models are possible with NIPCE and GP as most promising candidates.
- MV angle and radius have highest influence on hemodynamics biomarkers.
- GSA should be performed over a range of input parameter variation for more robustness.
- UQ of echocardiography measurements has a 5-30% of variation and reduction input uncertainty can drastically improve those values.

The methods presented herein have been summarized in the freely available tool **SASQUATCH** which can be applied to arbitrary input-output relationships for surrogate modeling, sensitivity analysis and uncertainty quantification in cardiac hemodynamics simulations.

Appendix

Additional results

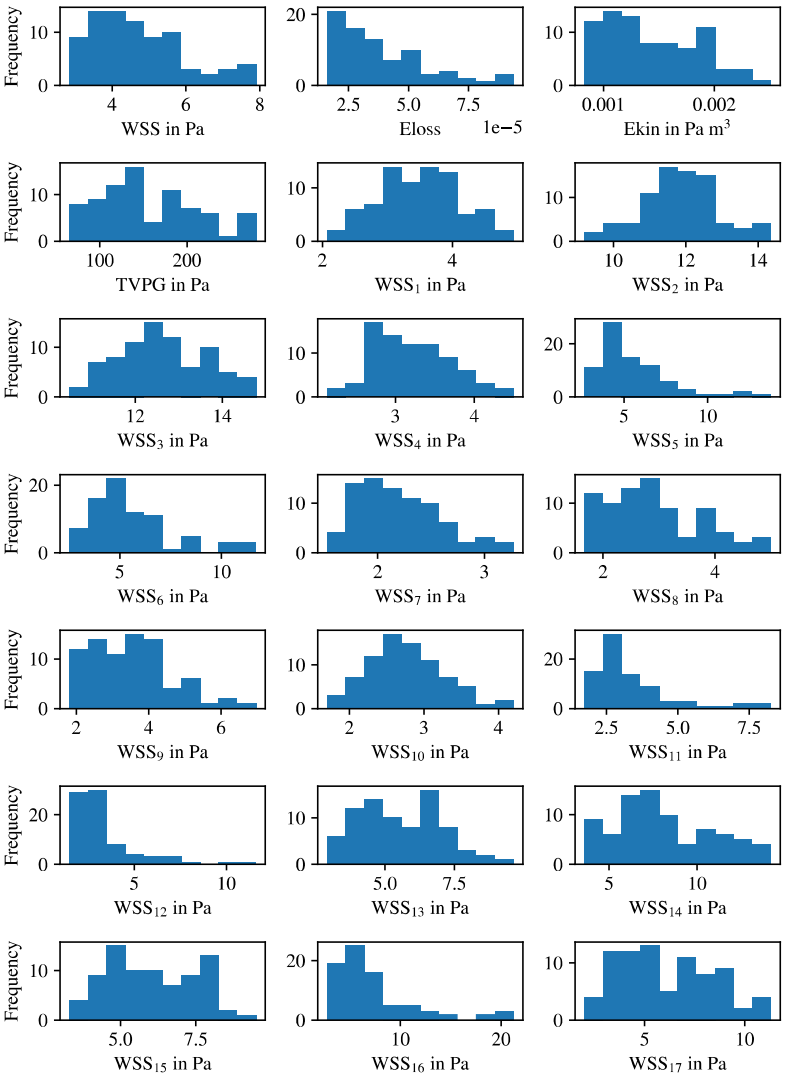

Fig. S1: Histograms of all output parameters.

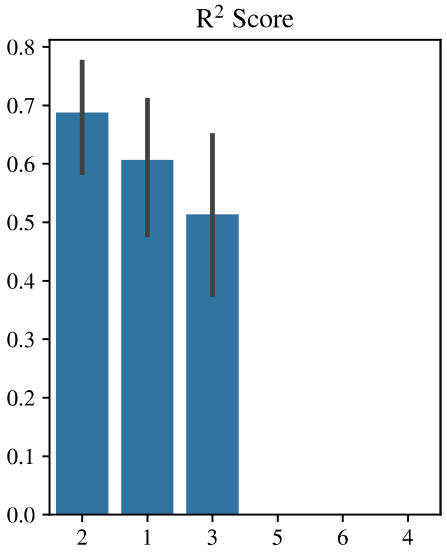

(a) Different orders for NIPCE.

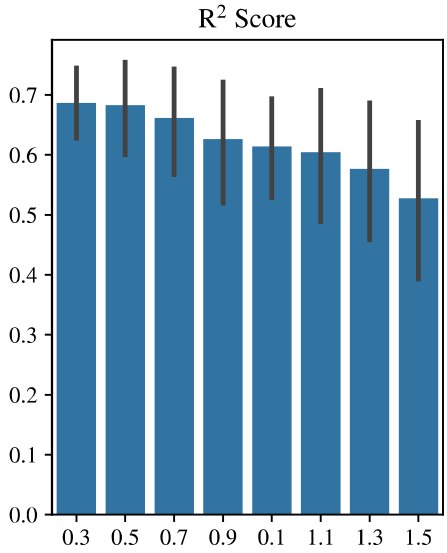

(b) Different values for ν for GP.

Fig. S2: Performance of *NIPCE* and *GP* with different configurations.

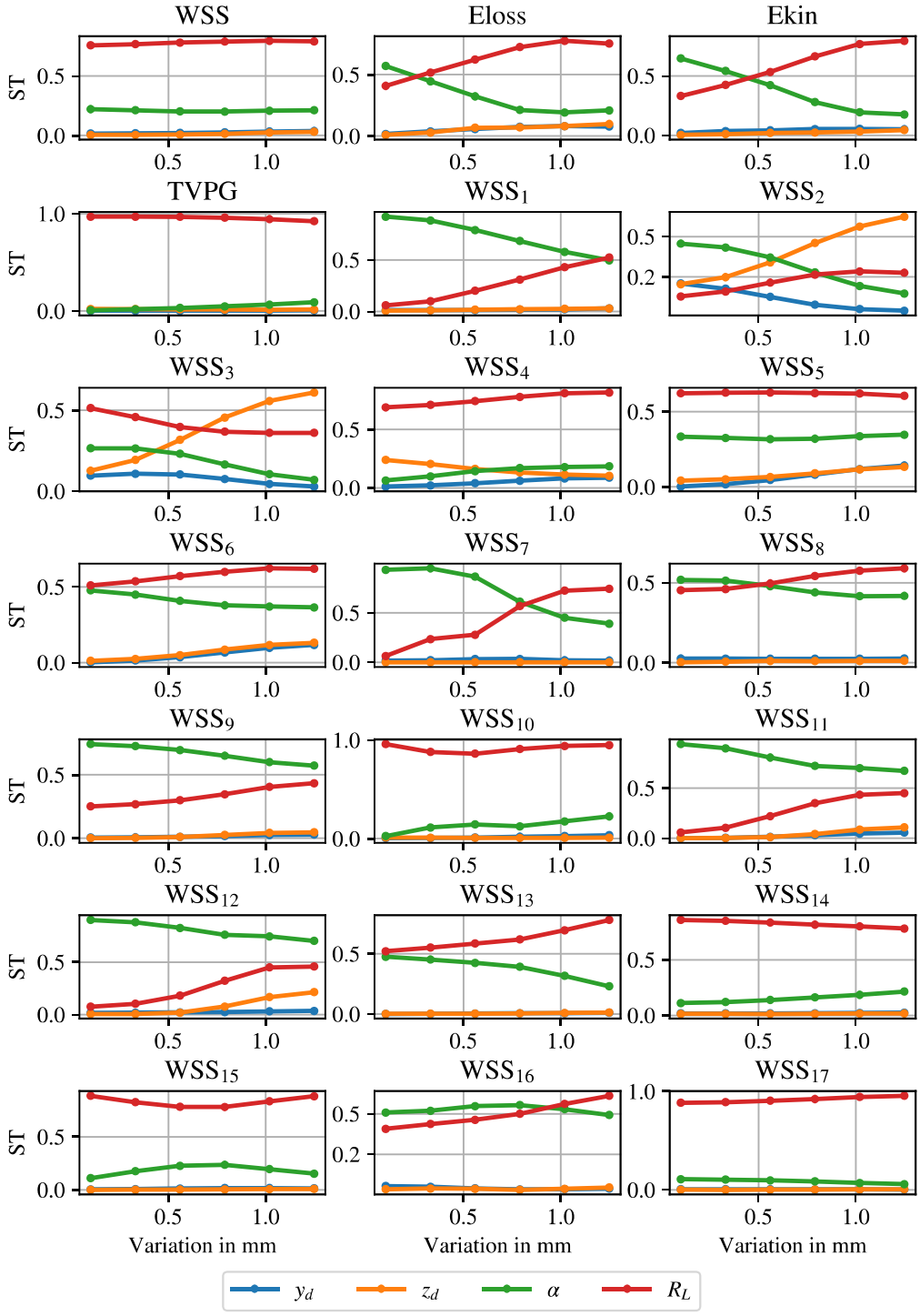

Fig. S3: Total order sensitivity values for all output parameters with varying input uncertainty in mm on the x-axes using *GP*.

Standard Deviation of Outputs

In Table S1 you can see the corresponding absolute standard deviation of variation in the outputs.

Output	**Input range in mm**					
	0.01	0.33	0.56	0.79	1.02	1.25
WSS_1	0.032	0.10	0.18	0.25	0.33	0.41
WSS_2	0.049	0.16	0.27	0.39	0.50	0.62
WSS_3	0.045	0.15	0.25	0.36	0.46	0.57
WSS_4	0.022	0.074	0.13	0.18	0.23	0.29
WSS_5	0.099	0.33	0.55	0.78	1.0	1.2
WSS_6	0.10	0.33	0.56	0.79	1.0	1.2
WSS_7	0.016	0.054	0.092	0.13	0.18	0.22
WSS_8	0.043	0.14	0.24	0.34	0.44	0.55
WSS_9	0.061	0.20	0.34	0.49	0.63	0.78
WSS_{10}	0.022	0.072	0.12	0.18	0.23	0.29
WSS_{11}	0.056	0.19	0.32	0.45	0.59	0.76
WSS_{12}	0.077	0.26	0.44	0.61	0.77	0.94
WSS_{13}	0.071	0.23	0.40	0.56	0.73	0.89
WSS_{14}	0.14	0.45	0.77	1.1	1.4	1.8
WSS_{15}	0.071	0.23	0.40	0.56	0.72	0.89
WSS_{16}	0.17	0.56	0.94	1.3	1.7	2.1
WSS_{17}	0.11	0.37	0.62	0.88	1.1	1.4
WSS	0.060	0.20	0.34	0.48	0.63	0.77
TVPG	2.7	8.8	15	22	28	35
E_{loss}	8.6×10^{-7}	2.8×10^{-6}	4.9×10^{-6}	6.9×10^{-6}	9.0×10^{-6}	1.1×10^{-5}
E_{kin}	2.0×10^{-5}	6.7×10^{-5}	1.1×10^{-4}	1.6×10^{-4}	2.1×10^{-4}	2.6×10^{-4}

Table S1: SD of outputs for input variation in mm.

Table S2 gives the same information as Table S1 but relative to each outputs mean.

Output	**Input range in mm**					
	0.01	0.33	0.56	0.79	1.02	1.25
WSS_1	0.96	3.17	5.39	7.64	9.90	12.20
WSS_2	0.41	1.36	2.32	3.28	4.26	5.24
WSS_3	0.36	1.19	2.02	2.86	3.71	4.56
WSS_4	0.76	2.51	4.26	6.02	7.77	9.52
WSS_5	2.28	7.47	12.40	17.04	21.30	25.19
WSS_6	2.12	6.97	11.69	16.14	20.43	24.42
WSS_7	0.77	2.54	4.35	6.22	8.15	10.16
WSS_8	1.54	5.09	8.65	12.24	15.87	19.54
WSS_9	1.72	5.71	9.74	13.87	18.11	22.50
WSS_{10}	0.79	2.63	4.51	6.46	8.50	10.62
WSS_{11}	2.20	7.24	12.00	16.42	20.69	24.95
WSS_{12}	2.82	9.29	15.48	20.89	25.49	29.82
WSS_{13}	1.29	4.25	7.20	10.16	13.13	16.09
WSS_{14}	1.60	5.30	9.09	13.04	17.20	21.66
WSS_{15}	1.16	3.83	6.51	9.21	11.93	14.67
WSS_{16}	3.09	10.07	16.45	22.02	26.97	31.38
WSS_{17}	1.85	6.11	10.37	14.63	18.89	23.15
WSS	1.40	4.60	7.79	10.95	14.04	17.02
TVPG	1.56	5.19	8.96	12.95	17.26	22.01
E_{loss}	2.69	8.85	14.91	20.77	26.38	31.55
E_{kin}	1.48	4.90	8.30	11.68	15.04	18.37

Table S2: SD of outputs in percent for input variation in mm.

References

[1] M. Abramowitz and I. A. Stegun. *Handbook of Mathematical Functions*. Dover, New York, 1965.

[2] A. M. Bavo, A. M. Pouch, J. Degroote, J. A. Vierendeels, J. H. Gorman, R. C. Gorman, and P. Segers. Patient-specific cfd models for intraventricular flow analysis from 3d ultrasound imaging: Comparison of three clinical cases. *Journal of biomechanics*, 50:144–150, 2017. doi:10.1016/j.jbiomech.2016.11.039.

[3] C. Blum, U. Steinseifer, and M. Neidlin. Systematic analysis of non-intrusive polynomial chaos expansion to determine rotary blood pump performance over the entire operating range. *Computers in Biology and Medicine*, 168:107772, 2023. doi:10.1016/j.compbiomed.2023.107772.

[4] C. Chnafa, C. Chnafa, S. Mendez, and F. Nicoud. Image-based simulations show important flow fluctuations in a normal left ventricle: What could be the implications? *Annals of Biomedical Engineering*, 44:3346–3358, 2016. doi:10.1007/s10439-016-1614-6.

[5] D. Collia, G. Libero, G. Pedrizzetti, and V. Ciriello. Surrogate models provide new insights on metrics based on blood flow for the assessment of left ventricular function. *Scientific Reports*, 12, 2022. doi:10.1038/s41598-022-12560-3.

[6] A. de Vecchi, A. Gómez, K. Pushparajah, T. Schaeffter, J. M. Simpson, R. Razavi, G. P. Penney, N. P. Smith, and D. A. Nordsletten. A novel methodology for personalized simulations of ventricular hemodynamics from noninvasive imaging data. *Computerized Medical Imaging and Graphics*, 51:20 – 31, 2016. doi:10.1016/j.compmedimag.2016.03.004.

[7] H. M. El-Husseiny, E. A. Mady, D. Ma, L. Hamabe, K. Takahashi, and R. Tanaka. Intraventricular pressure gradient: A novel tool to assess the post-infarction chronic congestive heart failure. *Frontiers in Cardiovascular Medicine*, 9, 2022. doi:10.3389/fcvm.2022.944171.

[8] M. S. M. Elbaz, R. J. van der Geest, E. E. Calkoen, A. de Roos, B. P. F. Lelieveldt, A. A. W. Roest, and J. J. M. Westenberg. Assessment of viscous energy loss and the association with three-dimensional vortex ring formation in left ventricular inflow: In vivo evaluation using four-dimensional flow mri. *Magnetic resonance in medicine*, 77(2):794–805, 2017. doi:10.1002/mrm.26129.

[9] N. Freidoonimehr, R. C. Chin, A. C. Zander, and M. Arjomandi. A review on the effect of temporal geometric variations of the coronary arteries on the wall shear stress and pressure drop. *Journal of biomechanical engineering*, 2021. doi:10.1115/1.4051923.

[10] A. Gruenwald, J. Korte, N. Blomeyer, C. Winkler, K. Linden, U. Herberg, S. Gross-Hardt, U. Steinseifer, and M. Neidlin. Intraventricular flow simulations in singular right ventricles reveal deteriorated washout and low vortex formation. *Cardiovascular Engineering and Technology*, 13, 2021. doi:10.1007/s13239-021-00598-9.

[11] T. Homma and A. Saltelli. Importance measures in global sensitivity analysis of nonlinear models. *Reliability Engineering & System Safety*, 52(1):1–17, 1996. URL: https://www.sciencedirect.com/science/article/pii/0951832096000026, doi:10.1016/0951-8320(96)00002-6.

[12] S. Hosder, R. Walters, and M. Balch. Efficient sampling for non-intrusive polynomial chaos applications with multiple uncertain input variables. *Proceedings of the 9th AIAA Non-Deterministic Approaches Conference*, 125, 2007. doi:10.2514/6.2007-1939.

[13] E. Karabelas, S. Longobardi, J. Fuchsberger, O. Razeghi, C. Rodero, M. Strocchi, R. Rajani, G. Haase, G. Plank, and S. Niederer. Global sensitivity analysis of four chamber heart hemodynamics using surrogate models. *IEEE Transactions on Biomedical Engineering*, PP:1, 2022. doi:10.1109/TBME.2022.3163428.

[14] S. S. Khalafvand, E. Y. K. Ng, L. Zhong, and T.-K. Hung. Three-dimensional diastolic blood flow in the left ventricle. *Journal of biomechanics*, 50:71–76, 2017. doi:10.1016/j.jbiomech.2016.11.032.

[15] A. Kheradvar, C. Rickers, D. Morisawa, M. Kim, G.-R. Hong, and G. Pedrizzetti. Diagnostic and prognostic significance of cardiovascular vortex formation. *Journal of cardiology*, 2019. doi:10.1016/j.jjcc.2019.05.005.

[16] R. M. Lang, L. P. Badano, V. Mor-Avi, J. Afilalo, A. da Costa Armstrong, L. Ernande, F. A. Flachskampf, E. Foster, S. A. Goldstein, T. Kuznetsova, P. Lancellotti, D. Muraru, M. H. Picard, E. R. Rietzschel, L. G. Rudski, K. T. Spencer, W. Tsang, and J.-U. Voigt. Recommendations for cardiac chamber quantification by echocardiography in adults: an update from the american society of echocardiography and the european association of cardiovascular imaging. *European heart journal cardiovascular Imaging*, 16 3:233–70, 2015. doi:10.1016/j.echo.2014.10.003.

[17] Y.-H. Loke, F. Capuano, V. Cleveland, J. G. Mandell, E. Balaras, and L. J. Olivieri. Moving beyond size: vorticity and energy loss are correlated with right ventricular dysfunction and exercise intolerance in repaired tetralogy of fallot. *Journal of Cardiovascular Magnetic Resonance*, 23(1):98, 2021. doi:10.1186/s12968-021-00789-2.

[18] J. O. Mangual, E. Kraigher-Krainer, A. D. Luca, L. Toncelli, A. M. Shah, S. D. Solomon, G. Galanti, F. Domenichini, and G. Pedrizzetti. Comparative numerical study on left ventricular fluid dynamics after dilated cardiomyopathy. *Journal of biomechanics*, 46 10:1611–7, 2013. doi:10.1016/j.jbiomech.2013.04.012.

[19] Y. Nakajima, T. Hozumi, K. Takemoto, S. Fujita, T. Wada, M. Kashiwagi, K. Shimamura, Y. Shiono, A. Kuroi, T. Tanimoto, T. Kubo, A. Tanaka, and T. Akasaka. Noninvasive estimation of impaired left ventricular untwisting velocity by peak early diastolic intra-ventricular pressure gradients using vector flow mapping. *Journal of Echocardiography*, 19:166 – 172, 2021. doi:10.1007/s12574-021-00520-1.

[20] G. Pedrizzetti, G. L. Canna, O. R. Alfieri, and G. Tonti. The vortex—an early predictor of cardiovascular outcome? *Nature Reviews Cardiology*, 11:545–553, 2014. doi:10.1038/nrcardio.2014.75.

[21] A. Puy, W. Becker, S. Lo Piano, and A. Saltelli. A comprehensive comparison of total-order estimators for global sensitivity analysis. *International Journal for Uncertainty Quantification*, 12, 2021. doi:10.1615/Int.J.UncertaintyQuantification.2021038133.

[22] C. J. Roy and W. Oberkampf. A comprehensive framework for verification, validation, and uncertainty quantification in scientific computing. *Computer Methods in Applied Mechanics and Engineering*, 200:2131–2144, 2011. doi:10.1016/j.cma.2011.03.016.

[23] D. Rutkowski, G. Barton, C. Francois, H. Bartlett, P. Anagnostopoulos, and A. Roldán-Alzate. Analysis of cavopulmonary and cardiac flow characteristics in fontan patients: Comparison with healthy volunteers. *Journal of Magnetic Resonance Imaging*, 49, 2019. doi:10.1002/jmri.26583.

[24] A. Santiago, C. Butakoff, B. Eguzkitza, R. A. Gray, K. May-Newman, P. Pathmanathan, V. Vu, and M. Vázquez. Design and execution of a verification, validation, and uncertainty quantification plan for a numerical model of left ventricular flow after lvad implantation. *PLoS Computational Biology*, 18, 2021. doi:10.1371/journal.pcbi.1010141.

[25] T. Schenkel, M. Malvè, M. Reik, M. Markl, B. Jung, and H. Oertel. Mri-based cfd analysis of flow in a human left ventricle: Methodology and application to a healthy heart. *Annals of Biomedical Engineering*, 37:503–515, 2009. doi:10.1007/s10439-008-9627-4.

[26] J. H. Seo, V. Vedula, T. P. Abraham, A. C. Lardo, F. Dawoud, H. chang Luo, and R. Mittal. Effect of the mitral valve on diastolic flow patterns. *Physics of Fluids*, 26:121901, 2014. doi:10.1063/1.4904094.

[27] M. Strocchi, S. Longobardi, C. M. Augustin, M. A. F. Gsell, A. Petras, C. A. Rinaldi, E. J. Vigmond, G. Plank, C. J. Oates, R. D. Wilkinson, and S. A. Niederer. Cell to whole organ global sensitivity analysis on a four-chamber heart electromechanics model using gaussian processes emulators. *PLOS Computational Biology*, 19, 2023. doi:10.1371/journal.pcbi.1011257.

[28] J.-N. Thiel, U. Steinseifer, and M. Neidlin. Generic framework for quantifying the influence of the mitral valve on ventricular blood flow. *International journal for numerical methods in biomedical engineering*, 2023. doi:10.1002/cnm.3684.

[29] H. S. Wong, B. Li, A. Tulzer, G. Tulzer, and C. H. Yap. Fluid mechanical effects of fetal aortic valvuloplasty for cases of critical aortic stenosis with evolving hypoplastic left heart syndrome. *Annals of Biomedical Engineering*, 51:1485 – 1498, 2023. doi:10.1007/s10439-023-03152-x.

[30] D. Zhao, G. Quill, K. Gilbert, V. Wang, H. Houle, M. Legget, P. Ruygrok, R. Doughty, J. Pedrosa, J. D'hooge, A. Young, and M. Nash. Systematic comparison of left ventricular geometry between 3d-echocardiography and cardiac magnetic resonance imaging. *Frontiers in Cardiovascular Medicine*, 8, 09 2021. doi:10.3389/fcvm.2021.728205.